



Parametric instabilities of a stratified shear layer

M. Ryan Buchta¹, Jason Yalim¹, Bruno D. Welfert¹ and Juan M. Lopez^{1,†}

¹School of Mathematical and Statistical Sciences, Arizona State University, Tempe, AZ 85287, USA

(Received 28 January 2021; revised 11 April 2021; accepted 21 April 2021)

A Boussinesq fluid inside a stably thermally stratified square container whose walls are inclined 45° with respect to gravity, with two opposite walls kept at constant temperatures and the other two insulated is nearly isothermal in the regions above and below the horizontal diagonal. The flow is concentrated in the wall boundary layers and a shear layer centred about the horizontal diagonal. The equilibrium is maintained by the balance between dissipation in the shear and boundary layers, the heat fluxes at the constant temperature walls, and the induced flow resulting from the no-flux condition at the inclined insulated walls. The dynamical response of the fluid to vertical oscillations of the container is studied over a range of forcing frequencies. For a small forcing amplitude and below a viscosity-dependent cutoff forcing frequency, this response exhibits a modal cellular structure localized about the shear layer. With increasing forcing amplitude, the response experiences instabilities, studied here numerically at a forcing frequency above the cutoff frequency, that are similar to those encountered in the Faraday wave problem, such as parametric subharmonic instability, triadic resonance and resonant collapse.

Key words: stratified flows, parametric instability

1. Introduction

Due to their ubiquitous presence in a wide range of geophysical flow phenomena, there is considerable interest in the instabilities of sheared density interfaces (Thorpe 1987; Fernando 1991; Ivey, Winters & Koseff 2008; Caulfield 2020, 2021). Much insight has been gained from studying three idealized settings (Sutherland 2010): when the density interface and the velocity shear layer coincide, Kelvin–Helmholtz instability leads to the interface rolling up into billows; when they do not coincide, Holmboe instability ensues with waves travelling in opposite directions either side of the density interface; and when there are two density interfaces subjected to shear, Taylor instability results in billows of a more complicated nature. These idealized flows are unidirectional (parallel) flows. The stability analysis as well as experimental investigations of these types of flows

† Email address for correspondence: juan.m.lopez@asu.edu

are problematic in that the initial density and shear profiles are not equilibrium states. This leads to compromises: the characteristic time scales for the evolution of the initial profiles and of their instabilities need to be carefully tuned in experiments, while linear stability analysis usually is based on the assumption that the so-called basic state is quasisteady, evolving on a slower diffusive time scale (Thorpe 1971; Parker, Caulfield & Kerswell 2020).

Container walls affect the flow in non-trivial ways. The consequences of walls at oblique angles to gravity were studied by Grayer *et al.* (2020) using a differentially heated square container with two opposite walls maintained at constant temperatures, one hot and the other cold, and the other two walls insulated. When the relative balance between buoyancy and viscous effects (quantified by the buoyancy number R_N) is sufficiently large, $R_N \gtrsim 10^3$, the flow splits into three distinct regions, a central region with nearly linear vertical temperature variation delimited by lines emanating from the horizontal corners impinging on the opposite walls. With increasing R_N , the flow tends to be isothermal above and below these lines, hot in the top region and cold in the bottom region, and the velocity tends to zero everywhere except in wall boundary layers and in thin shear layers about the lines emanating from the horizontal corners and separating the three regions. The situation at tilt angle 45° is special as the shear layers emanating from the two horizontal corners coincide. The flow is stable, steady and consists of two triangular essentially isothermal stagnant regions surrounded by wall boundary layers and separated by a stratified shear layer.

In the present study, we explore the response of the 45° tilt state to parametric forcing consisting of vertical oscillations of the tilted container. This type of parametric forcing was previously studied for the 0° tilt case, where the unforced state is a static equilibrium with stable linear stratification (Yalim, Lopez & Welfert 2018; Yalim, Welfert & Lopez 2019*a,b*; Yalim, Lopez & Welfert 2020). Those studies were motivated by the experiments of Benielli & Sommeria (1998), who considered vertical oscillations of stratified fluids in a rectangular cavity; they considered both a two-layer system and a linearly stratified system. In both, they found the response flows to be dominated by parametric resonances, but the details differed substantially between the two. The two-layer system had many analogies with the well-studied Faraday wave problem (Benjamin & Ursell 1954; Miles & Henderson 1990; Kumar & Tuckerman 1994). Most studies of the Faraday wave problem involve two immiscible fluids, but there is also much interest in the parametric forcing of two-layer systems of miscible fluids (Zoueshtiagh, Amiroudine & Narayanan 2009; Briard, Gréa & Gostiaux 2019; Briard, Gostiaux & Gréa 2020). A major distinction between the Faraday problem with miscible and immiscible fluids is that in the immiscible case the jump discontinuity at the density interface is sufficient for instability, whereas for the miscible case the density varies smoothly throughout and a sufficiently large localized density gradient is needed for instability. In both cases, when the container is rectilinear with walls parallel or orthogonal to gravity, the unforced state is static and the stratifying agent in the miscible case diffuses vertically (parallel to gravity). In contrast, the 45° tilt case has flow even in the absence of forcing, primarily in the wall boundary layers and the horizontal shear layer separating the top and bottom regions, which are essentially isothermal with a thin smooth variation of temperature (and hence density) across the shear layer. The responses to vertical oscillatory accelerations have much in common with the miscible Faraday flows, although there exist notable differences due to the presence of a shear flow at the interface separating the isothermal regions.

2. Governing equations, symmetries and numerics

Consider a fluid of kinematic viscosity ν , thermal diffusivity κ and coefficient of volume expansion β contained in a square cavity of side lengths L . The opposite walls of the

Parametric instabilities of a stratified shear layer

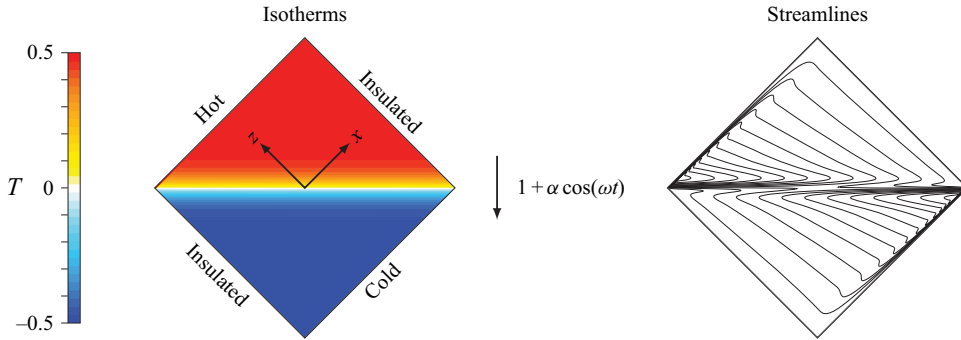


Figure 1. Schematic of the forced system, with isotherms and streamlines of the unforced state at $R_N = 10^{5.5}$, and the temperature colourmap for $T \in [-0.5, 0.5]$. The streamlines are plotted using 14 linearly spaced isolevels in the range $0 \leq \psi \leq 1.6 \times 10^{-4}$, where ψ is the streamfunction, such that $u = -\partial\psi/\partial z$ and $w = \partial\psi/\partial x$.

cavity are insulated and the other two opposite walls are held at fixed temperatures, T_+ and T_- , with $\Delta T = T_+ - T_- > 0$. The cavity is oriented such that its walls make a 45° angle with the downward directed gravity g . The non-dimensional temperature is $T = -0.5 + (T^* - T_-)/\Delta T$, where T^* is the dimensional temperature. Length is scaled by L and time by $1/N$, where $N = \sqrt{g\beta\Delta T/L}$. A Cartesian coordinate system $\mathbf{x} = (x, z) \in [-0.5, 0.5] \times [-0.5, 0.5]$ is attached to the cavity with its origin at the centre and the directions x and z aligned with the sides, with associated velocity $\mathbf{u} = (u, w)$. A schematic is shown in [figure 1](#).

The cavity is subjected to harmonic vertical oscillations of amplitude α and frequency ω . In the cavity reference frame, all walls are no-slip with boundary condition $\mathbf{u} = \mathbf{0}$, on the insulated walls $\partial T/\partial x|_{x=\pm 0.5} = 0$ and on the conducting walls $T|_{z=\pm 0.5} = \pm 0.5$. Under the Boussinesq approximation, the governing equations are

$$\left. \begin{aligned} \partial \mathbf{u} / \partial t + \mathbf{u} \cdot \nabla \mathbf{u} &= -\nabla p + (1 + \alpha \cos \omega t) T \hat{\mathbf{e}} + R_N^{-1} \nabla^2 \mathbf{u}, & \nabla \cdot \mathbf{u} &= 0, \\ \partial T / \partial t + \mathbf{u} \cdot \nabla T &= (Pr R_N)^{-1} \nabla^2 T, \end{aligned} \right\} \quad (2.1)$$

where $\hat{\mathbf{e}} = (1/\sqrt{2}, 1/\sqrt{2})$, p is the pressure and $R_N = NL^2/\nu$ is the buoyancy number. The Prandtl number $Pr = \nu/\kappa = 0.71$ is fixed and variations in R_N , ω and α are explored.

In the absence of any other external force, this system admits a stable steady flow solution (\mathbf{u}_s, p_s, T_s) , whose characteristic features are described in Grayer *et al.* (2020). When subjected to vertical oscillations of sufficiently small amplitude α , the forced response flow is synchronous with the forcing frequency. The system is also centrosymmetric, invariant to a reflection through the origin $\mathcal{C} : (\mathbf{u}, T)(x, z, t) \mapsto (-\mathbf{u}, -T)(-x, -z, t)$.

The governing equations are solved numerically with a spectral-collocation code used in related studies (Yalim *et al.* 2019b, 2020; Grayer *et al.* 2020). Chebyshev polynomials of degree 201×201 were used for all cases except for the largest forcing amplitude case $\alpha = 0.3$, which used 601×601 resolution. The number of time steps per forcing period varied with ω , with 1000 time steps per period for $\omega = 0.7$, and the time step remained approximately independent of ω .

3. Small amplitude forcing

For sufficiently small forcing amplitude α , the response flow is a synchronous centrosymmetric limit cycle L_1 . This response flow is quantified by the square of the

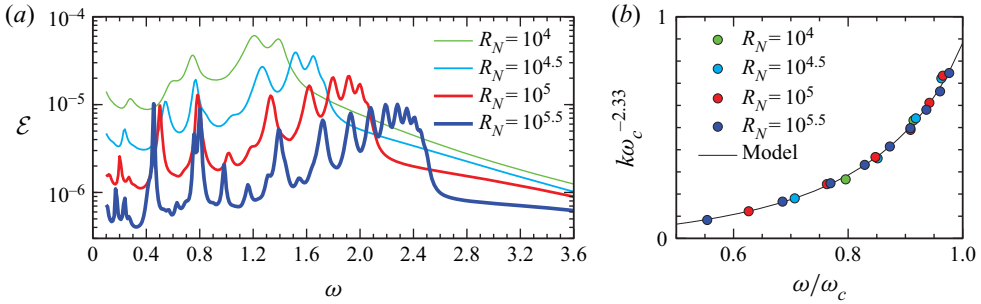


Figure 2. (a) Response diagram, \mathcal{E} vs ω , and (b) spatial wavenumber k of Θ , scaled by $\omega_c^{2.33}$, vs ω , scaled by ω_c , for $\alpha = 0.01$ and R_N as indicated. The cutoff frequency is $\omega_c = 0.4R_N^{0.145}$ and the model used in (b) is $k\omega_c^{-2.33} = 0.15(\omega/\omega_c)^2/[1 - 0.83(\omega/\omega_c)]$.

L_2 -norm of the temperature deviation from the unforced steady state, $\Theta = T - T_s$, scaled by the forcing amplitude and averaged over one forcing period,

$$\mathcal{E} = \frac{\omega}{2\pi} \int_0^{2\pi/\omega} \int_{-0.5}^{0.5} \int_{-0.5}^{0.5} \frac{\Theta^2}{\alpha^2} dx dz dt. \quad (3.1)$$

Figure 2(a) shows how \mathcal{E} varies with ω for $\alpha = 0.01$ and various R_N . The response curves $\mathcal{E}(\omega)$ for each R_N were determined from individual simulations at discrete values of $\omega = 0.01j$ for $j = 10$ to 360 in steps of 1, using the unforced steady state at that R_N as the initial condition for each simulation. Additional ω cases near the main peaks were computed for refinement of the response curves at the two largest R_N values. The time-averaging to obtain \mathcal{E} was done over one forcing period after transients had died off sufficiently, i.e. when the periodically strobed \mathcal{E} converged to machine precision (typically after several thousand forcing periods, depending on ω , and with more periods needed for larger R_N).

For any given R_N , \mathcal{E} exhibits broad peaks up to a cutoff frequency ω_c , beyond which \mathcal{E} drops off sharply. As R_N is increased, existing peaks sharpen and new ones appear, while the response levels between peaks are proportional to R_N^{-1} . On the other hand, the response levels at peaks corresponding to $\omega \lesssim 1$ appear to plateau and then increase with R_N , hinting at possible resonances in this regime, although all responses remain small relative to the forcing amplitude even at the highest $R_N = 10^{5.5}$ considered here. The peaks shift towards lower values of ω for $\omega \lesssim 1$, whereas for $\omega \gtrsim 1$ they shift to larger ω up to ω_c , which increases with R_N as $\omega_c \approx 0.4R_N^{0.145}$.

To gain insight into the response \mathcal{E} , snapshots of Θ of the response flows at the peaks in figure 2 are shown in figure 3 for $R_N = 10^{5.5}$ and $\alpha = 0.01$. These snapshots illustrate how the perturbations are localized in the central stratified shear layer. All snapshots are at a phase where they are maximal in the interior of the cavity, except for the last two ($\omega = 2.55$ and 3.50), for which the response is focused at the horizontal corners. The peak responses are synchronous, approximately standing waves with a small horizontal drift, and consist of cells along the shear layer and their size decreases with increasing ω . Moreover, away from the container walls, these centrosymmetric responses have approximate up-down and left-right reflection symmetries; supplementary movie 1 shows animations over one forcing period.

Responses Θ associated with peaks at forcing frequencies $\omega \lesssim \omega_c$ are characterized by a single row of similar cells (excluding corner contributions) with an even wavenumber k . Their wavenumber increases with increasing ω , as illustrated by the sequence of snapshots corresponding to $1.39 \leq \omega \leq 2.45 (\approx \omega_c \text{ for } R_N = 10^{5.5})$ in rows two and three of figure 3.

Parametric instabilities of a stratified shear layer

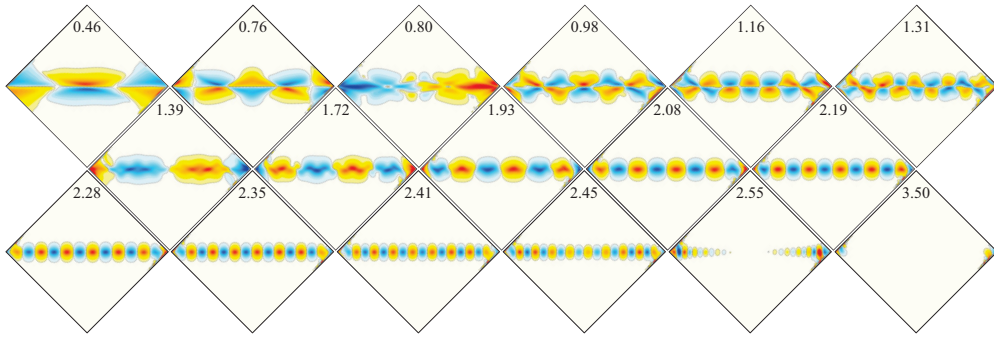


Figure 3. Snapshots of Θ at $R_N = 10^{5.5}$, $\alpha = 0.01$ and indicated ω corresponding to the peaks in figure 2. See supplementary movie 1 available at <https://doi.org/10.1017/jfm.2021.373> for animations over one forcing period.

Figure 2(b) shows that the relationship between k and ω for different R_N collapses onto a single curve under appropriate scalings by a power of ω_c . In the model used in figure 2(b), $k \omega_c^{-2.33} = 0.15(\omega/\omega_c)^2/[1 - 0.83(\omega/\omega_c)]$, k increases quadratically with ω for small ω/ω_c , as is to be expected from a basic dispersion analysis, but the increase is somewhat faster than quadratic as $\omega \rightarrow \omega_c$. Note that while such a model suggests that the scaling by ω_c aligns the peaks of the response curves obtained for different R_N in figure 2(a) for ω close to ω_c , it does not provide a good alignment for peaks in the lower ω range.

The Θ response at $\omega = 0.80$ in the first row of figure 3 appears to be anomalous. It seems to share more features with peak responses at larger ω than with other peak responses in the same row. This can be reconciled by considering the development of the peaks as R_N is increased. Figure 4 illustrates how several of the dominant peak responses evolve as R_N varies from 10^4 to $10^{5.5}$. Rows one and three show how the responses at $\omega = 0.46$ and $\omega = 1.39$, obtained at $R_N = 10^{5.5}$, inherit their spatial characteristics from responses at lower R_N for slightly detuned forcing frequencies, with a compression in the vertical direction due to increased buoyancy. The second row of figure 4 addresses the disparity of the $\omega = 0.80$ response at $R_N = 10^{5.5}$, showing how the two peak responses at $\omega = 0.76$ and $\omega = 0.80$ originate from a broader peak response at lower R_N and detuned ω . In particular, the Θ response at $R_N = 10^5$ and $\omega = 0.78$ (shown at maximal phase) includes signatures of both the $\omega = 0.76$ and $\omega = 0.80$ peak responses at $R_N = 10^{5.5}$, with a strong horizontal response emanating from the horizontal corners, together with bicorn-shaped cells in the centre of the cavity (see supplementary movie 2 for animations over one forcing period). Such splitting of peaks in response diagrams is expected as viscous effects are reduced and the separation between different modal responses increases.

4. Large amplitude forcing

The stability of L_1 is now considered as the forcing amplitude α is increased for $\omega = 3.6 > \omega_c$ at $R_N = 10^5$. The responses are quantified by the Nusselt numbers at the hot (+) and cold (−) walls:

$$Nu_{\pm}(t) = \int_{-0.5}^{0.5} \partial T / \partial z|_{z=\pm 0.5} dx. \quad (4.1)$$

A measure of the flow asymmetry, $\mathcal{A} = (Nu_+ - Nu_-)/(Nu_+ + Nu_-)$, is zero for centrosymmetric responses; response flows for $\alpha \leq 0.09$ are centrosymmetric.

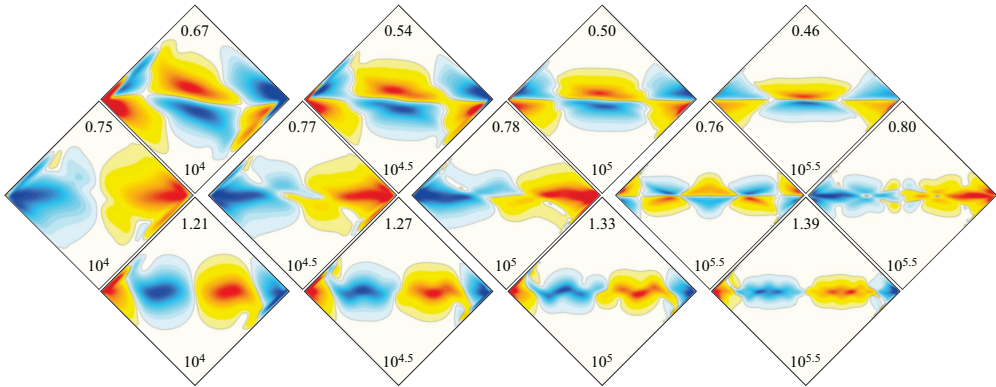


Figure 4. Snapshots of Θ for two sequences associated with response peaks in figure 2 at increasing R_N (indicated at the bottom of each frame) and peak ω (top corner of frames). See supplementary movie 2 for animations over one forcing period.

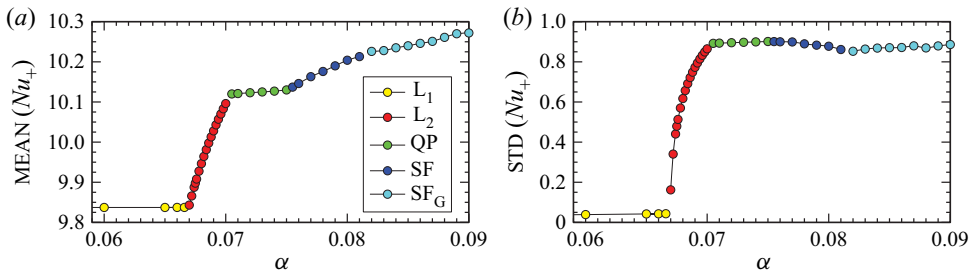


Figure 5. Variations with α of the mean and the standard deviation of the Nusselt number, $\text{MEAN}[Nu_+]$ and $\text{STD}[Nu_+]$, for $R_N = 10^5$ and $\omega = 3.6$.

For the unforced case $\alpha = 0$, $Nu_+ \approx 9.84$. Figure 5 shows the mean and standard deviation of Nu_+ as α is increased. For $\alpha \lesssim 0.067$, L_1 is a stable centrosymmetric limit cycle; it has small amplitude (characterized by $\text{STD}[Nu_+]$) and the time average $\text{MEAN}[Nu_+]$ only slightly increases with α . At $\alpha \approx 0.0675$, L_1 loses stability to another centrosymmetric limit cycle, denoted L_2 , whose frequency is $\omega/2 = 1.80$. This instability is a parametric subharmonic instability: the spatial structure of L_2 corresponds to that of L_1 at $\omega = 1.80$. The time series of Nu_+ over several forcing periods for L_1 at $\alpha = 0.066$ and L_2 at $\alpha = 0.068$ are shown in figure 6(a), and supplementary movie 3 animates the temperature deviation Θ of these two limit cycles, along with that of L_1 at $\omega = 1.80$ and $\alpha = 0.1$, highlighting the correspondence between L_2 at $\omega = 3.60$ and L_1 at $\omega = 1.80$.

At $\alpha \approx 0.0702$, L_2 loses stability via a Neimark–Sacker bifurcation (Kuznetsov 2004), spawning a centrosymmetric quasiperiodic response flow denoted QP. The Nu_+ time series of QP at $\alpha = 0.073$ is also shown in figure 6(a). Fourier transforms over 10^4 forcing periods of this time series, as well as of QP at $\alpha = 0.0705$ and 0.0751 , have peaks at frequencies $\omega_1 = 1.80$, $\omega_2 = 1.31$ and $\omega_3 = 0.49$, with the power spectral densities at ω_2 and ω_3 being two orders of magnitude smaller than that at ω_1 . The relation $\omega_1 = \omega_2 + \omega_3$ is suggestive of a triadic resonance. Figure 7 shows a snapshot of QP at $\alpha = 0.073$, together with three Fourier modes M_1 , M_2 and M_3 , which are obtained by filtering QP

Parametric instabilities of a stratified shear layer

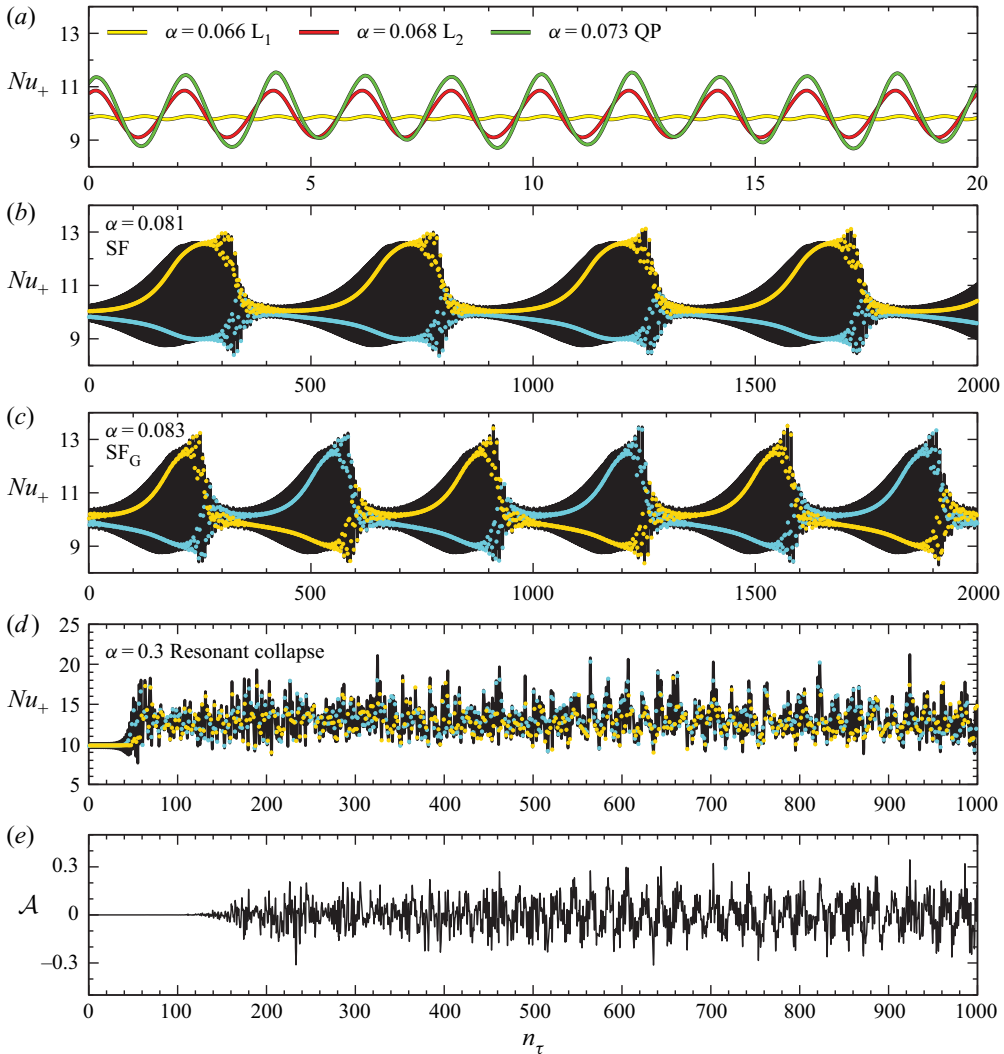


Figure 6. (a–d) Time series of Nu_+ for response flows at $R_N = 10^5$, $\omega = 3.6$ and α as indicated. The time series in (b–d) also include two two-period stroboscopes, taken one forcing period apart at forcing phase π . (e) The asymmetry measure \mathcal{A} for the resonant collapse case in (d).

at frequencies ω_1 , ω_2 and ω_3 :

$$M_k(x, z) = \frac{\omega_k}{2\pi} \int_0^{2\pi/\omega_k} T(x, z, t) \sin(\omega_k t + \phi) dt, \quad (4.2)$$

where $\phi \in [0, \pi]$ maximizes $\|M_k\|_\infty$, for $k = 1, 2$, or 3 . These modes have cellular structures with 1, 2 and 3 cells in the vertical and 6, 9 and 3 cells in the horizontal localized along the shear layer (see supplementary movie 4). The relations $2 + 1 = 3$ and $9 - 6 = 3$ between the cell numbers of M_1 , M_2 and M_3 confirm the spatial resonance and the triadic nature of QP. Here, M_1 is similar to L_2 at lower α , and M_2 is similar to L_1 at forcing frequency ω_2 . However, M_3 is not similar to the L_1 response at ω_3 . This is typical of triadic resonances, where one of the two free modes is from a different set to those directly resonated by the forcing (Lopez & Marques 2018; Wu, Welfert & Lopez 2020).

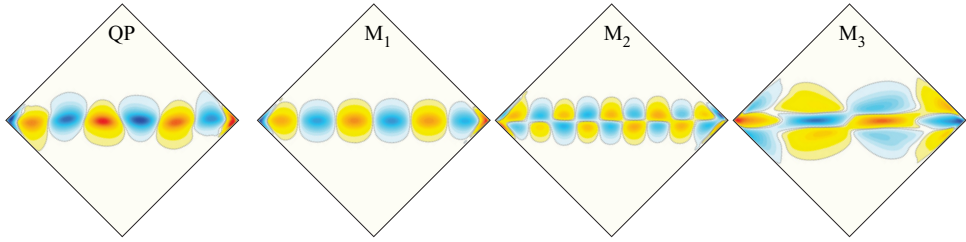


Figure 7. Snapshot of Θ for QP at $\alpha = 0.073$, $\omega = 3.6$ and $R_N = 10^5$, together with its leading Fourier modes, M_1 , M_2 and M_3 . See supplementary movie 4 for an animation over 20 forcing periods.

At $\alpha \approx 0.0752$, QP becomes unstable via another Neimark–Sacker bifurcation introducing a very low frequency of order 0.01. The flow response is similar to that of QP, with amplitude slowly increasing until the oscillations in the isotherms about the horizontal shear layer interact with the walls near the two horizontal corners. When this happens, there are fast reflections along the shear layer that destroy the coherence of the QP-like oscillations, resulting in a relatively fast collapse toward a state resembling L_2 at lower α . Following this collapse, the slow build-up of the QP-like oscillations are reinstated, followed by another collapse. All the while, the flow remains centrosymmetric. This slow-fast state is denoted SF. Figure 6(b) shows a time series of SF at $\alpha = 0.081$ in black, together with a pair of two-period stobes, in yellow and cyan, one forcing period apart at forcing phase π . The SF is stable up to $\alpha \approx 0.0813$, although there are small α windows where it is less regular with the intervals between collapses not being uniform. A characteristic of SF is that one of the two-period stobes of Nu_+ consistently tracks to the high-end of Nu_+ while the other two-period strobe consistently tracks to the low-end of Nu_+ .

For $\alpha > 0.081$, the response is also slow-fast, but the two-period stobes of Nu_+ interchange tracking to the low-end and high-end of Nu_+ following each collapse. This is a type of gluing bifurcation, very similar to that reported and discussed in Yalim *et al.* (2019b) for the parametrically forced system at 0° tilt. This glued slow-fast response is denoted SF_G . Figure 6(c) shows the time series of Nu_+ together with the pair of two-period stobes for SF_G at $\alpha = 0.083$.

As α is further increased beyond 0.083, the long periods between the fast collapses have irregular durations, and the two-period stobes tracking to the low-end and high-end of Nu_+ switch in an apparently random fashion. With increasing α , the peak value of Nu_+ before collapses increases. Also, following a collapse the flow is more energetic, with larger Nu_+ for larger α . Figure 6(d) shows the time series of Nu_+ at $\alpha = 0.3$. The initial condition at $t = 0$ is the unforced $R_N = 10^5$ state which is impulsively forced at $\alpha = 0.3$ and $\omega = 3.6$. The initial transient is like the slow ramp-ups in SF and SF_G , but following the first collapse after approximately 50 forcing periods the flow does not relax towards L_2 , and instead exhibits more energetic chaotic dynamics, akin to the resonant collapse in a precessionally forced rotating cylinder (McEwan 1970). Snapshots of the isotherms at various times (denoted by the number of forcing periods, n_τ , following the impulsive start) are shown in figure 8.

Accompanying figure 8 are a number of movies showing temporal evolutions of the isotherms over select intervals. The first of these, supplementary movie 5a, shows the slow ramp-up followed by the initial collapse over $n_\tau \in [30, 60]$. Even during the wave-breaking events after $n_\tau \approx 50$, the flow appears to retain centrosymmetry; see the sequence of snapshots from the movie shown in the top two rows of figure 8. However, the asymmetry

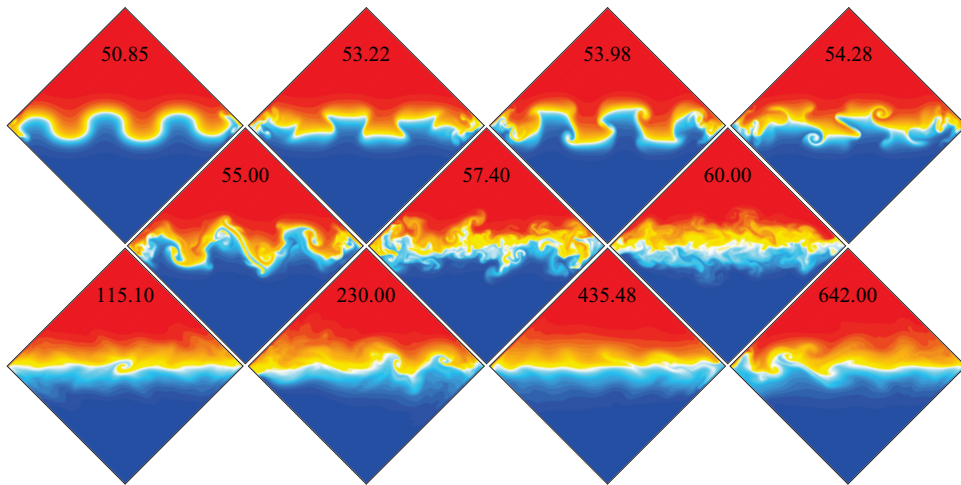


Figure 8. Snapshot of isotherms at the indicated number of forcing periods, n_τ , following an impulsive start to forcing with $\alpha = 0.3$ and $\omega = 3.6$ at $R_N = 10^5$. Animations covering a variety of time intervals are shown in supplementary movies 5a to 5e.

measure \mathcal{A} grows exponentially until saturating at $n_\tau \approx 170$ (see figure 6e), at which point the asymmetry is visually apparent in the isotherms. The next movie, supplementary movie 5b, covering $n_\tau \in [95, 125]$ shows two waves near the horizontal corners being excited while the centre remains relatively static. These break and then a Kelvin–Helmholtz-like roll-up forms at the origin at $n_\tau \approx 115$ (see figure 8). Supplementary movie 5c covers $n_\tau \in [220, 240]$. Larger amplitude Faraday wave-like L_2 oscillations occur at one corner and undergo wave breaking, followed by the formation of sharp undulations that travel horizontally, reminiscent of Holmboe waves. There is also a global sloshing motion, or seiche, with a period of approximately 20 forcing periods, that is most evident in the isotherms away from the central shear region. This period is clearly identifiable in the time series in figure 6(d,e) after 600 forcing periods. In supplementary movie 5d, covering $n_\tau \in [425, 455]$, the flow exhibits small-scale cusp-like convective mushrooms travelling towards both horizontal corners. The structures on the hot side of the shear layer travel to the hot corner while those on the cold side travel to the cold corner. Near the end of the animation a roll-up similar to a Kelvin–Helmholtz mushroom appears at the cold corner followed by an L_2 -like excitation of the shear layer. Finally, supplementary movie 5e, covering $n_\tau \in [625, 665]$, shows the build-up of Faraday wave-like oscillations that then develop into either left or right travelling waves. As the waves crash into a horizontal corner, there is mixing with the fluid in the interior. The sequence of events in the various movies bears a striking resemblance with the experimental movies of Faraday wave instabilities with miscible fluids in Briard *et al.* (2020).

5. Summary and conclusions

The responses to vertical parametric modulation of gravity of a fluid in a square container tilted at 45° , with two differentially heated opposite walls and two adiabatic opposite walls, are surprisingly very similar to those from a Faraday wave experiment, in spite of major differences existing in the set-ups. Whereas in the Faraday problem the unforced equilibrium is static, here it is non-trivial, consisting of wall boundary layers and a shear layer centred about the horizontal diagonal separating two near isothermal regions. It is

maintained by heat fluxes that are focused near the corners on either side of the shear layer. For sufficiently small forcing amplitudes, there is a forced centrosymmetric synchronous response.

Below a certain viscosity-dependent cutoff forcing frequency, the forced responses have modal cellular structure in the shear layer. Differences in their organization, in particular with respect to parities and symmetries, seem to be connected to the orientation of the forcing. Although gravity is only modulated vertically, the obliqueness of the container walls induces a horizontal component of the forcing whose effects combine with those due to the vertical forcing. The results in Grayer *et al.* (2021) indicate that one may expect the non-trivial forced responses at low forcing amplitude to be attributed to this horizontal forcing. Analysis of these different contributions and their interactions will be addressed elsewhere.

Above this cutoff frequency, the forced response is localized at the horizontal corners. Increasing the forcing amplitude at such a frequency leads to parametric subharmonic resonance, much like in the Faraday wave problem. At larger forcing amplitudes, the subharmonic response flow excites a pair of lower frequency modes in a triadic resonance. The identification of such a triadic resonance in a non-uniformly stratified shear flow is novel. Further increases in forcing amplitude lead to low-frequency modulations of the triadic response, resulting in a slow-fast resonant collapse scenario. The slow phase consists of the triadic response growing in amplitude until the response flow in the shear layer interacts with the container walls and, in particular, the horizontal corners. Then, there is a relatively fast collapse and the process repeats. With increasing forcing amplitude, the slow-fast dynamics become more complicated but the flow remains centrosymmetric, with the time-dependent heat fluxes at the hot and cold walls being identical. At much larger forcing amplitude, the response is no longer centrosymmetric, with different heat fluxes at the hot and cold walls. This difference leads to periods of time lasting many forcing periods during which the interior has an excess/deficit of thermal energy, culminating when the Faraday waves with cold/hot fluid encroach on the hot/cold wall as they come crashing near the left/right horizontal corner of the container.

The present configuration provides a relatively simple set-up for generating Faraday waves and studying their instabilities, including triadic resonances and other nonlinear interactions. In particular, it defines a framework for studying the transfer of energy between scales and the effects of shear in non-uniformly stratified flows, which may prove useful in furthering the understanding of these processes in the ocean and the atmosphere.

Supplementary movies. Supplementary movies are available at <https://doi.org/10.1017/jfm.2021.373>.


Acknowledgements. The authors thank ASU Research Computing facilities for computing resources.

Declaration of interests. The authors report no conflict of interest.

Author ORCIDs.

 M. Ryan Buchta <https://orcid.org/0000-0003-3194-316X>;

 Jason Yalim <https://orcid.org/0000-0001-6866-9833>;

 Bruno D. Welfert <https://orcid.org/0000-0002-9134-2078>;

 Juan M. Lopez <https://orcid.org/0000-0002-4580-6505>.

REFERENCES

- BENIELLI, D. & SOMMERIA, J. 1998 Excitation and breaking of internal gravity waves by parametric instability. *J. Fluid Mech.* **374**, 117–144.

Parametric instabilities of a stratified shear layer

- BENJAMIN, T.B. & URSELL, F. 1954 The stability of the plane free surface of a liquid in vertical periodic motion. *Proc. R. Soc. Lond. A* **225**, 505–515.
- BRIARD, A., GOSTIAUX, L. & GRÉA, B.-J. 2020 The turbulent Faraday instability in miscible fluids. *J. Fluid Mech.* **883**, A57.
- BRIARD, A., GRÉA, B.-J. & GOSTIAUX, L. 2019 Harmonic to subharmonic transition of the Faraday instability in miscible fluids. *Phys. Rev. Fluids* **4**, 044502.
- CAULFIELD, C.P. 2020 Open questions in turbulent stratified mixing: do we even know what we do not know? *Phys. Rev. Fluids* **5**, 110518.
- CAULFIELD, C.P. 2021 Layering, instabilities, and mixing in turbulent stratified flows. *Annu. Rev. Fluid Mech.* **53**, 113–145.
- FERNANDO, H.J.S. 1991 Turbulent mixing in stratified fluids. *Annu. Rev. Fluid Mech.* **23**, 455–493.
- GRAYER, H., YALIM, J., WELFERT, B.D. & LOPEZ, J.M. 2020 Dynamics in a stably stratified tilted square cavity. *J. Fluid Mech.* **883**, A62.
- GRAYER, H. II, YALIM, J., WELFERT, B.D. & LOPEZ, J.M. 2021 Stably-stratified square cavity subjected to horizontal oscillations: responses to small amplitude forcing. *J. Fluid Mech.* **915**, A85.
- IVEY, G.N., WINTERS, K.B. & KOSEFF, J.R. 2008 Density stratification, turbulence, but how much mixing? *Annu. Rev. Fluid Mech.* **40**, 169–184.
- KUMAR, K. & TUCKERMAN, L.S. 1994 Parametric instability of the interface between two fluids. *J. Fluid Mech.* **279**, 49–68.
- KUZNETSOV, Y.A. 2004 *Elements of Applied Bifurcation Theory*, 3rd edn. Springer.
- LOPEZ, J.M. & MARQUES, F. 2018 Rapidly rotating precessing cylinder flows: forced triadic resonances. *J. Fluid Mech.* **839**, 239–270.
- MCEWAN, A.D. 1970 Inertial oscillations in a rotating fluid cylinder. *J. Fluid Mech.* **40**, 603–640.
- MILES, J. & HENDERSON, D.M. 1990 Parametrically forced surface-waves. *Annu. Rev. Fluid Mech.* **22**, 143–165.
- PARKER, J.P., CAULFIELD, C.P. & KERSWELL, R.R. 2020 The viscous Holmboe instability for smooth shear and density profiles. *J. Fluid Mech.* **896**, A14.
- SUTHERLAND, B.R. 2010 *Internal Gravity Waves*. Cambridge University Press.
- THORPE, S.A. 1971 Experiments on the instability of stratified shear flows: miscible fluids. *J. Fluid Mech.* **46**, 299–319.
- THORPE, S.A. 1987 Transitional phenomena and the development of turbulence in stratified fluids: a review. *J. Geophys. Res.* **92**, 5231–5248.
- WU, K., WELFERT, B.D. & LOPEZ, J.M. 2020 Precessing cube: resonant excitation of modes and triadic resonance. *J. Fluid Mech.* **887**, A6.
- YALIM, J., LOPEZ, J.M. & WELFERT, B.D. 2018 Vertically forced stably stratified cavity flow: instabilities of the basic state. *J. Fluid Mech.* **851**, R6.
- YALIM, J., LOPEZ, J.M. & WELFERT, B.D. 2020 Parametrically forced stably stratified flow in a three-dimensional rectangular container. *J. Fluid Mech.* **900**, R3.
- YALIM, J., WELFERT, B.D. & LOPEZ, J.M. 2019a Modal reduction of a parametrically forced confined viscous flow. *Phys. Rev. Fluids* **4**, 103903.
- YALIM, J., WELFERT, B.D. & LOPEZ, J.M. 2019b Parametrically forced stably stratified cavity flow: complicated nonlinear dynamics near the onset of instability. *J. Fluid Mech.* **871**, 1067–1096.
- ZOUESHTIAGH, F., AMIROUDINE, S. & NARAYANAN, R. 2009 Experimental and numerical study of miscible Faraday instability. *J. Fluid Mech.* **628**, 43–55.